Journal of Solid State Chemistry 262 (2018) 264–272

Contents lists available at ScienceDirect

Journal of Solid State Chemistry

journal homepage: www.elsevier.com/locate/jssc

Investigation of the nanoscale two-component ZnS-ZnO heterostructures by means of HR-TEM and X-ray based analysis

I.A. Pankin[a,b,*], O.E. Polozhentsev[a], M.A. Soldatov[a], A.L. Bugaev[a,b], A. Tsaturyan[d], K.A. Lomachenko[c], A.A. Guda[a], A.P. Budnyk[a], C. Lamberti[a,e], A.V. Soldatov[a]

[a] The Smart Materials Research Center, Southern Federal University, Sladkova 178/24, 344090 Rostov-on-Don, Russia
[b] Department of Chemistry and NIS Interdepartmental Center, University of Torino, via Giuria 7, I-10125 Torino, Italy
[c] European Synchrotron Radiation Facility, 71 Avenue des Martyrs, CS 40220, 38043 Grenoble Cedex 9, France
[d] Institute of Physical and Organic Chemistry, Southern Federal University, Stachki Av. 194/2, Rostov-on-Don, Russian Federation
[e] Department of Physics, INSTM Reference Center and CrisDi Interdepartmental Center for Crystallography, University of Torino, via Giuria 1, I-10125, Torino, Italy

ARTICLE INFO

Keywords:
Microwave assisted synthesis
Semiconductor heterostructures ZnS/ZnO
Local atomic structure
Synchrotron radiation
X-ray powder diffraction
X-ray absorption spectroscopy
HERFD-XANES
Valence-to-core XES
HR-TEM
EDX

ABSTRACT

This article is devoted to the spectroscopic characterization of ZnS-ZnO nanoscale heterostructures synthesized by the microwave-assisted solvothermal method. The synthesized samples were investigated by means of X-ray powder diffraction (XRPD), high energy resolution fluorescence detected X-ray absorption near-edge-structure (HERFD-XANES) spectroscopy, valence-to-core X-ray emission spectroscopy (VtC-XES) and high resolution transmission electron microscopy (HR-TEM) as well as energy dispersive X-ray spectroscopy (EDX). The average crystallite size estimated by the broadening of XRPD peaks increases from 2.7 nm to 3.7 nm in the temperature range from 100 °C to 150 °C. HR-TEM images show that nanoparticles are arranged in aggregates with the 60–200 nm size. Theoretical estimation shows that the systems synthesized at higher temperatures more prone to the agglomeration. The full profile Reitveld analysis of XRPD data reveals the formation of hexagonal zinc sulfide structure, whereas electron diffraction data reveal also the formation of cubic zinc sulfide and claim the polymorphous character of the system. High energy resolution Zn K-edge XANES data unambiguously demonstrate the presence of a certain amount of the zinc oxide which is likely to have an amorphous structure and could not be detected by XRPD. Qualitative analysis of XANES data allows deriving ZnS/ZnO ratio as a function of synthesis temperature. EDX analysis depicts homogeneous distribution of ZnS and amorphous ZnO phases across the conglomerates. A complementary element-selective valence to core X-ray emission spectroscopy evidences formation of two-component system and confirms estimations of ZnS/ZnO fractions obtained by linear combination fit of XANES data.

1. Introduction

Nanotechnology provides a big potential for biomedical and pharmacological applications [1–5]. By decreasing the size of semiconducting material the novel properties appear due to the increase of surface/bulk ratio and quantum confinement effects [6–17]. Nanoscale semiconductor objects such as quantum dots and quantum wires represent a special class of inorganic luminophores and have high photostability as well as particularly interesting fluorescence properties: the emission wavelength depends strongly on the particle size and the nature of the material.

The main advantages of this kind of nanomaterials include high emission quantum yields, broad absorption spectra, size-tunable emission spectra, and good resistance to chemical and photochemical degradation [6]. The charge carriers inside the nanoscale semiconductors are confined in all three dimensions by the surface and thus the size and shape of nanoscale semiconductors determine the energy spectrum of electronic levels [6]. The possibility to tune the energy gap between electronic levels by changing the size of quantum dots (QDs) offers the great potential for applications in nanoelectronics, quantum computing, light emitters and solar cell systems [18–20].

During the last few years, many methods have been developed to produce ZnS QDs and heterostructures, such as synthesis in aqueous phase [21], sol-gel method [22,23], polyol method [24], solvo-hydrothermal synthesis [25], biosynthesis [10] and microwave-assisted solvothermal (MAS) method [26]. Among these methods, the MAS is

* Corresponding author at: The Smart Materials Research Center of Southern Federal University, Sladkova 178/24 st., 344090 Rostov-on-Don, Russia.
E-mail address: ilya.punk.in@google.com (I.A. Pankin).

https://doi.org/10.1016/j.jssc.2018.03.008
Received 30 December 2017; Received in revised form 28 February 2018; Accepted 5 March 2018
Available online 17 March 2018
0022-4596/

particularly attractive because of several advantages: rapid heating of the reaction mixture, low reaction temperature, reduction of the synthesis time, and the possibility to control the overall particle morphology, size, and aggregation process [27–29].

The synthesized colloidal QDs (generally uncapped) are relatively unstable and encounter the difficulties in dispersion and preservation [30]. Possible existing of the surface states significantly reduces the electron-hole recombination rate, lowering the luminescent quantum yield [30]. The possible way to overcoming this problem is to further cap the bare QDs with another material, forming a core-shell configuration. By choosing a core and shell compounds, their morphological and optical properties can be easily tuned to suit for various applications.

The most represented in the literature the core-shell structures are based on the ZnO core and ZnS shell [30–33]. Conversely, a few studies reported the inverted ZnS/ZnO core-shell QDs [34–36].

Most of the studies on the ZnS/ZnO heterostructures focus on two- [9,37] or one- and zero-dimensional heterostructures [38]. The nanoscale ZnS material is a non-toxic, metastable and can be easily oxidized [39,40]. The ZnO material has a very high binding energy as well as good chemical and thermal stability. The ZnO shell can protect the ZnS core and introduce multiple functionalities that the single composite ZnS structure cannot possess.

Due to the high penetration depth of hard X-rays and element selectivity of the technique, X-ray absorption spectroscopy (XAS) [41,42] can be applied in situ for structural and electronic characterization of nanoscale semiconductor heterostructures such as core-shell quantum dots, quantum wires or very thin nanofilms and nanoparticles in their colloidal form, supported on a substrate or incapsulated inside a solid matrix [6,15,43]. Moreover, the local nature of the technique makes XAS spectroscopy a powerful tool to investigate samples without long-range atomic order such as dilute magnetic semiconductors [44,45], amorphous materials [46–48], liquids [49,50], active sites of various catalysts [41,51–56], biological objects [57], etc. Recently it has been shown that XAS spectroscopy is able to monitor minor changes of structural parameters in the proximity of X-ray absorbing doping atoms for doped QDs of II-VI group [58,59].

X-ray emission spectroscopy (XES) is a powerful technique to characterize the metal sites in a plenty of different kind of condensed materials including nano-dimensional systems such as nanowires, nanotubes, nanoparticles and so on [43,60–67]. Valence to core XES (VtC-XES) signal corresponds to the transitions of the electrons from the occupied valence orbitals to the core level with a vacancy, created by an incident X-ray photon [68].

Combination of X-ray diffraction and absorption studies has been shown to provide complementary long-/short-range information [69], particularly relevant in the case of NPs with a core-shell structure with the average size of 2 – 3 nm [41], where both techniques are informative.

This work is aimed to study the structural topology of the two component ZnS-ZnO heterostructures synthesized by microwave assisted synthesis (MAS) approach. Obtained precipitate is characterized by small ZnS NPs capped by truly amorphous ZnO phase which fills interstitial space upon agglomeration process. The effect of the MAS temperature on the kinetic of NPs formation is under the scope of this study.

2. Experimental details

2.1. Synthesis

Commercially available $Zn(CH_3COO)_2{\cdot}2H_2O$ (99.9%), thiourea (TM) and ammonium hydroxide solution (28–30%) (Sigma Aldrich) and ethanol were used. Doubly distilled water was used throughout. All chemicals were used without further purification.

The samples under study were prepared using the MAS method at various temperature (100 °C, 120 °C and 150 °C) for 20 min in accordance with a protocol developed in a previous study [58]. The synthesis is described as follows: initially, 7.5 μmol of thiourea was dissolved in 9 ml of a water-ethanol (1:1) solution (solution 1). Then 2.5 μmol of $Zn(CH_3COO)_2{\cdot}2H_2O$ was dissolved in another 9 ml of a water-ethanol (1:1) solution to obtain the solution 2. The solution 2 was then quickly mixed with the solution 1 under vigorous stirring. The resulting pH was 7.1. 1 ml of concentrated ammonium hydroxide solution was then slowly added until the pH value arrived at 10.2. According ref [70] at this value of pH there is a maximum solubility of zinc hydroxide. During the reaction pH of solution decreased to 9.7. Resulting colorless solution was placed in the microwave system Discover SP (CEM Corp.) and heated for various temperature (100 °C, 120 °C and 150 °C), with the maximum power set to 150 W and pressure set to 300 PPI. After completion, the solution was cooled in the microwave with a stream of room temperature air. The white precipitate was wash out by water-ethanol solution and centrifuged three times at 20,000 rpm for 15 min. The samples were dried at 60 °C for overnight.

2.2. XRPD

X-ray powder diffraction (XRPD) patterns were obtained using laboratory Bruker D2 PHASER diffractometer, exploiting Cu $K\alpha_{1,2}$ radiation (λ_1 = 1,5405(1) Å, λ_2 = 1,5443(3) Å). The voltage and current of the X-ray tube were set as 30 kV and 10 mA, respectively. XRPD patterns were measured in the 2θ range from 20° to 80° with 0.02° step. Full-profile analysis of XRPD patterns was performed by means of Jana2006 software [71].

2.3. HR-TEM and EDX

High-resolution Transmission Electron Microscopy (HR-TEM) images were obtained using a FEI Technai G2, F20 operated at 200 kV. Element analysis was performed by means of EDAX Octane Silicon Drift Detector. Measurements were performed after the samples were dispersed in isopropanol and then dried.

2.4. HERFD-XANES

The HERFD-XANES spectra were recorded at the ID26 beamline of ESRF (Grenoble, France). Cryogenically-cooled fixed-exit double-crystal monochromator Si(311) with an energy resolution $\Delta E/E = 0.3 \times 10^{-4}$ was employed to obtain monochromatic X-ray beam. To collect HERFD XANES and XES spectra we used emission spectrometer equipped with five spherically bent analyzer crystals operating in the energy range 4.5–17 keV. This way of detecting provides extremely high energy resolution $\Delta E/E < 0.001$. While collecting HERFD-XANES data the energy window of emission spectrometer was centered to the position of Zn $K\beta_{1,3}$ emission line.

In a fluorescence mode the self-absorption effects could significantly affect the shape of the spectra [72,73], especially for concentrated samples. Boron nitride powder was used to dilute samples for minimization of self-absorption effect keeping reasonable signal to noise ratio. The powder of preliminary dried samples was mixed with a BN and pressed into pellets (approximately 9 mg of samples powder was mixed with 90 mg of BN) with 1.3 cm^2 surface area. The pellets were placed to the sample holder and the collimated X-ray beam.

The high photon flux delivered by the three undulators available on the ID26, combined by the beamline focusing optics, provides a very intense and highly collimated X-ray beam that requires radiation damage tests to be carefully performed. For this aim, for each sample, we have measured 15 fast and short scans before the normal ones (See Supp. info Fig S1). In addition, to prevent any radiation degradation of the samples and inhomogeneous effects, we have collected the data from the different spots on the same pellets every time moving to the

"fresh" point and collecting 10 HERFD-XANES scans for each spot. The resulting spectrum for each sample was obtained by averaging over all measurements at one spot and at different spots for each sample. After each 5 HERFD-XANES scans one longer scan (including EXAFS region) was collected on each spot for the sake of more reliable XANES normalization and qualitative analysis of k^2 weighted FT signal.

2.5. VtC-XES

VtC-XES data were also collected at ID26 beamline of ESRF. The excitation energy was set up to 9.80 keV. The same fluorescence spectrometer as described above (see Section 2.4) was used for the detection of X-ray emission signal. The emission of K$\beta_{1,3}$ main line and K$\beta_{2,5}$ lines were detected in the energy range from 9.55 keV to 9.59 keV and from 9.58 to 9.70 keV, respectively. Final spectrum was obtained by averaging 2–3 scans of K$\beta_{2,5}$ spectra for each sample collected on the different spots on the pellet. The TFY (Total Fluorescence Yield) signal was used for the normalization of VtC-XES data obtained for the samples with a different amount of Zn. Background signal was removed using Voigt function interpolation [74].

3. Results and discussion

3.1. Reaction process

The overall reaction process during the MW treatment can be described as following. In colorless solution, the major fraction corresponds to the zinc cations - $Zn(OH)_4^{2-}$ [75]. Meanwhile since the pH is increased due to addition of the ammonium hydroxide solution the formation of the zinc ammine complexes takes place. The formation of the colorless solution can be thus described by two reactions [76]:

$$Zn_{(aq)}^{2+} + nOH_{(aq)}^{-} \leftrightarrow [Zn(OH)_{n(aq)}]^{2-n} \quad (1)$$

$$Zn_{(aq)}^{2+} + nNH_{3(aq)} \leftrightarrow [Zn(NH_3)_{n(aq)}]^{2+} \quad (2)$$

where n varies from 1 to 4 and is the same for reactions 1–4. In the beginning of MW treatment, the zinc hydroxide complexes pass to the amorphous $Zn(OH)_2$ phase which leads to the formation of the ZnO after drying of the product. At the same time, the hydrolysis of the thiourea occurs in the reaction mixture. The reaction proceeds by the action of the OH^- ions present in the alkaline solution resulting in the formation of H_2NCN and HS^-, followed by the neutralization of the latter to give rise to free S^{2-} ions, according to following reaction [77]:

$$(NH_2)_2CS + 2OH^- \rightarrow H_2CN_2 + S^{2-} + 2H_2O \quad (3)$$

The free sulfide anions react with zinc complexes and form ZnS by the reaction:

$$[Zn(OH)_{n(aq)}]^{2-n}/[Zn(NH_3)_{n(aq)}]^{2+} + S_{(aq)}^{2-} \rightarrow nOH^-_{(aq)}/nNH_{3(aq)} + ZnS_{(s)} \quad (4)$$

The mechanism of the ZnS formation including a hydrolysis of the thiourea was intensively discussed in the works of Hodes [78] and Markov [79].

The limiting stage of the ZnS formation depends on the processes involving the hydrolysis of the thiourea because the equilibrium constant of this reaction has the smallest value compared to all the processes that take place in the reaction mixture.

3.2. XRPD analysis

XRPD patterns were collected for the whole series of the synthesized samples. Fig. 1 shows the experimental XRPD patterns and calculated contribution from hexagonal ZnS phase. XRPD patterns for each sample are characterized by several peaks corresponding to

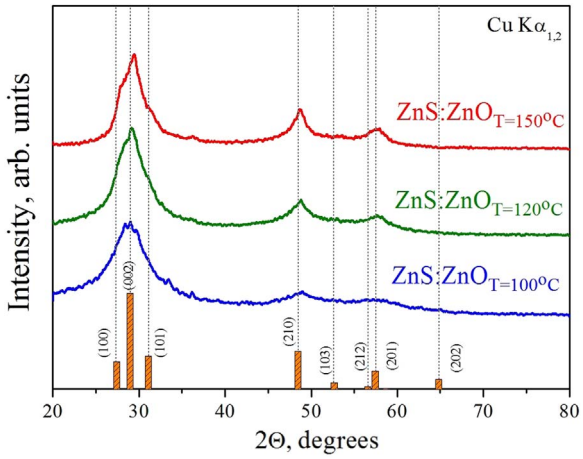

Fig. 1. XRPD patterns of ZnS:ZnO samples synthesized by MAS method at 150, 120, and 100 °C (upper, middle, and bottom patterns, respectively). Columns below the diffraction patterns correspond to the position of the theoretical reflections for hexagonal ZnS. (For interpretation of the references to color in this figure legend, the reader is referred to the web version of this article.)

hexagonal zinc sulfide ZnS phase; among them, the most intense ones are the (100), (002) and (101) reflections localized in 27° – 30° 2θ interval. Due to small crystallite size, Bragg reflections are significantly broadened (FHWM ~ 3° in 2θ)., which results in overlapping of the peaks and makes XRPD patterns of the samples similar to the ones of cubic ZnS [80]. However full-profile Retvield analysis evidences the hexagonal ZnS (space group *P63mc*) with (100), (002) and (101) reflections localized at 27.3°, 29.0° and 31.1°, respectively [80].

The crystallite sizes were estimated using Debye-Scherrer [81–83] equation for FWHM of XRPD peaks obtained as a result of full-profile analysis assuming the spherical shape of the particles (nanocrystallites). It was found that crystallite size of different samples is in the range from 2.7 nm to 3.7 nm and that it increases with increasing temperature of the microwave assisted synthesis T_{MAS}, (see Table 1 below). Higher temperature affects the particle nucleation and favors formation of larger particles in solution. The results of full-profile Retvield analysis are summarized in the Table S1 of SI. No evidence of crystalline by-product phases was obtained. However, formation of amorphous phases, including surface species, cannot be excluded based solely on XRPD analysis.

3.3. HR-TEM

For the samples synthesized at 120 °C and 150 °C high resolution TEM images with low and high magnifications were obtained (Figs. 2a and 2b, respectively). Low magnification image shows a group of agglomerates of NPs with a size distribution in the 60–200 nm range. These agglomerates consist of small nanoparticles as evidences from XRPD profile analysis. High magnification HR-TEM images confirms this conclusion, showing that on the scale 5–10 nm one observe regions with differently oriented atomic planes which are also match with the XRPD estimation of the crystallite size. The surface region of the high magnification TEM image also shows layered morphology.

Fig. 2(c) reports the electron diffraction collected for the sample synthesized at 120 °C. Three well pronounced rings with a different radius in reciprocal space clearly demonstrate that samples under the study have polycrystalline nature. The most bright 1st diffraction ring could be referred to (0;0;–2) and (1;1;1) interatomic planes of ZnS_{hex} and ZnS_{cub} nanocrystallites respectively, oriented in a random way with respect to the electron beam. However, there are no traces of reflections from (0;1;2) and (–1;1;2) interatomic planes of hexogonal ZnS. Electron diffraction analysis shows that more dim 2nd and 3rd rings most likely correspond to the cubic phase of zinc sulfide (See Section 2 of SI).

Table 1
The results of LCF Zn K-edge XANES analysis and estimation of amorphous oxidized layer thickness.

Sample	T,°C	$r_{core}^{(ZnS)}$, nm	LCF XANES results		Agglomeration number, n
			(ZnS)	(ZnO)	
ZnS:ZnO$_{T=100C}$	100	1.35	0.57	0.43	199
ZnS:ZnO$_{T=120C}$	120	1.75	0.69	0.31	434
ZnS:ZnO$_{T=150C}$	150	1.85	0.77	0.23	513

Taking into consideration the above suggested hypothesis that small ZnS NPs undergo agglomeration and form relatively big agglomerates we have estimated the effect of the synthesis temperature on the agglomeration process. Agglomeration number specifies the number of primary particles or molecular units in a single conglomerate of a given size [84]. Considering a spherical shape of NPs, agglomeration number was calculated employing the following expression [85]:

$$n = \frac{4\pi r^3 N_a}{3V_M} \quad (5)$$

where n is the agglomeration number, N_a is Avogadro's number ($6.22 \cdot 10^{23}$ mol^{-1}), r is the nanoparticle radius calculated according to the XRPD peaks broadening and V_m is the molar volume of ZnS in cm^3 mol^{-1}. The molar volume is defined as:

$$V_m = \frac{M_{ZnS}}{\rho} \quad (6)$$

where M_{ZnS} is the molar mass and ρ is the density of hexagonal ZnS (4.023 g/cm^3). The calculated agglomeration numbers are reported in Table 1. The obtained results (see Table 1) reveal that NPs synthesized at higher temperatures agglomerate more effectively reaching agglomeration number n = 513 for the sample synthesized at 150 °C.

3.4. EDX analysis

Energy dispersive analysis (EDX) was performed for the samples synthesized at 120 °C and 150 °C using EDAX Octane Silicon Drift Detector. Element-selective mapping was performed for the square area with a dimension ~ 4 × 4 and 2 × 2 μm for the samples synthesized at 120 °C and 150 °C, respectively (See Fig. 3).

EDX analysis shows homogeneous distributions of oxygen and sulfur atoms across relatively big conglomerates of NPs. One observes only relatively small ~ 1 μm^2 sulfur poor region highlighted with a white rectangle in Fig. 4. The concentrations of different element Zn:S:O are following 55:27:18 at% and 45:31:21 at% for the samples synthesized at 120 °C and 150 °C, respectively. Considering that all O and S atoms interact with Zn, the ratios ZnS:ZnO derived by EDX analysis are 67:33 and 60:40 for the samples synthesized at 120 °C and 150 °C, respectively. These values are in a good agreement with ratios of ZnS/ZnO obtained by means of XANES linear combination fit (See Section 3.5).

3.5. HERFD-XANES

The small size of the crystallites limits the informativity of the XRPD data. Therefore we have also employed XANES and EXAFS spectroscopies and VtC-XES for a detailed investigation of the local atomic structure of the samples under study.

Fig. 5 reports the HERFD-XANES spectra collected for the samples synthesized by MAS method at different temperatures in comparison with the data obtained for reference bulk samples: hexagonal ZnS and ZnO (We used wurtzite type ZnS as a reference compounds taking into account that full profile XRPD analysis provides the best fit for hexagonal ZnS). The XANES features for NPs are broader and thus less pronounced with respect to those present in the corresponding spectra of the reference crystalline compounds. This spectroscopic evidence reflects the small particle size which are involved in agglomeration and the high disorder parameters provided by local defects in NPs (that implies a significant fraction of Zn atoms at the surface or interface between different crystallites forming the same conglomerate). In addition their broader nature the HERFD-XANES spectra of all the samples can be reproduced by the spectra of ZnS and ZnO model compounds. Indeed, NPs exhibit the sharp feature in the range 9663–9667 eV typical of ZnS (peak "B" of black curve in the inset) and the broadened feature in the range 9667 – 9672 eV typical of ZnO (feature "C" of the grey curve in the inset). Moreover, the first resonance after the edge (peak A) in the NPs occurs at the energy (9662.6 eV) that is intermediate between that observed for ZnS (9662.2 eV) and ZnO (9663.1 eV) model compounds. The spectroscopic evidences reported in Fig. 5 are the clear proofs of the coexistence of both a crystalline ZnS phase, detected in the XRPD study (see Fig. 1), and of an amorphous ZnO phase that escaped XRPD detection, being observable by local XAS spectroscopy.

Three HERFD-XANES spectra collected for NPs are characterized by two isosbestic points at ~ 9665 and ~ 9673 eV testifying that the relative fraction of the ZnS and ZnO phases in samples under the study is different.

XANES spectra were used to quantify the fraction of the two phases in the three different samples. In this regard, we computed a series of

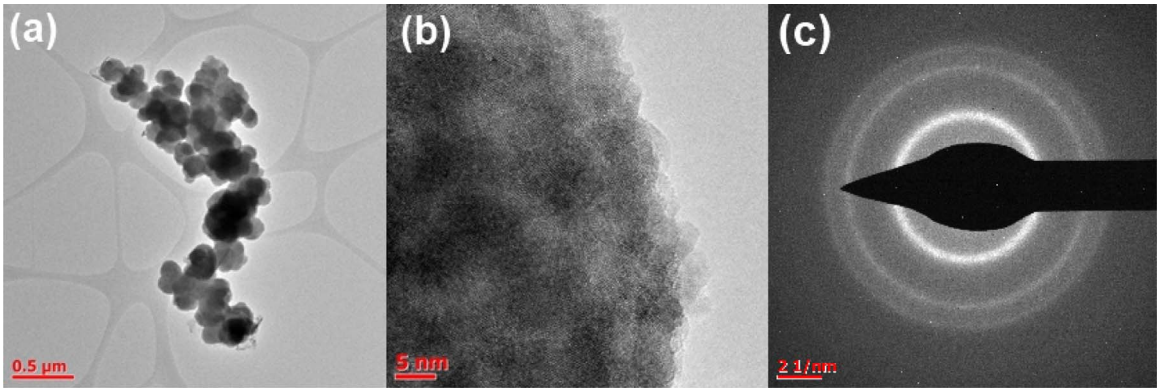

Fig. 2. (a) Low- and **(b)** high-magnification HR-TEM image, and **(c)** electron diffraction pattern collected for the sample synthesized at 120 °C.

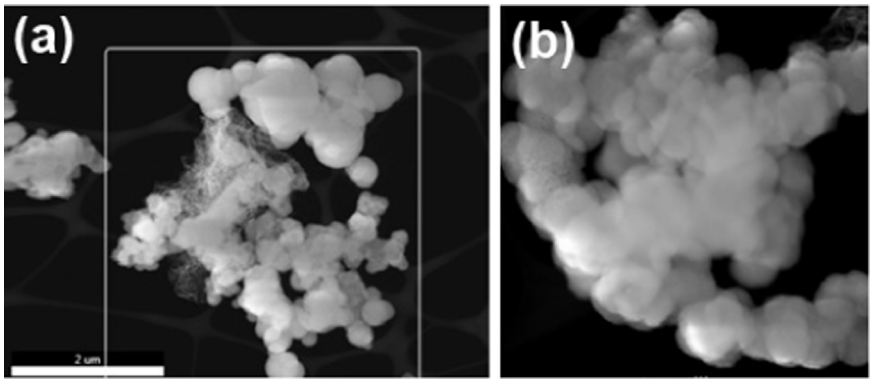

Fig. 3. STEM images obtained for the samples synthesized (a) at 120 °C and (b) 150 °C.

theoretical spectra obtained by linear combination (LC) of the experimental spectra of ZnS and ZnO model compounds, see Fig. 6a. The main XANES features (A, B, C, D, E, F in the Fig. 6a) clearly undergo a progressive energy shift and/or intensity change as a function of the relative fraction of the two phases. It is notable that the same trends are observed in the experimental HERFD-XANES spectra collected for these samples (Fig. 3b) and this trend is unambiguously related to a different amount of oxide and sulfide components in the samples. Moreover: (i) the red shift of the peak A; (ii) increase of the peak B intensity; (iii) damping of the peak C intensity; and (iv) well pronounced energy shift and intensity increase of the broad post edge feature F, reveal for the synthesis at different temperature the progressive increase of the relative fraction of ZnS phase to the detriment of the ZnO one upon increasing T_{MAS} (follow the arrows in both parts of Fig. 3). The only exception to this trend is made for features D and E, well defined in the spectra of the model compounds (Fig. 3a), that are however lost in the spectra collected on ZnS:ZnO samples (Fig. 3b) because of the broadening caused by the nanometric size of the samples.

For quantitative analysis of the ZnO amount in the samples, a Linear Combination Fit (LCF) for the HERFD-XANES data collected on the samples synthesized at different temperatures was employed in DEMETER Athena software [86]. HERFD-XANES spectra of reference bulk ZnO and ZnS samples were considered as principal components. The result of LCF analysis quantifies the gradual increase of the relative fraction of the sulfide phase as a function of T_{MAS} (See Table 1). In this regard, it is worth remembering that from XRPD analysis (see Section 3.2), we found that also the size of the ordered ZnS phase gradually increase with T_{MAS}. For the sample with a smaller particle size (~2.6 nm) roughly equivalent amount of sulfide and oxide phases was obtained, while for the samples with a larger particle size (~ 3.5 and ~ 3.7 nm) the concentration of ZnS phase is significantly higher and reaches the highest value of about ~77% for the sample synthesized at 150 °C (See Table 1).

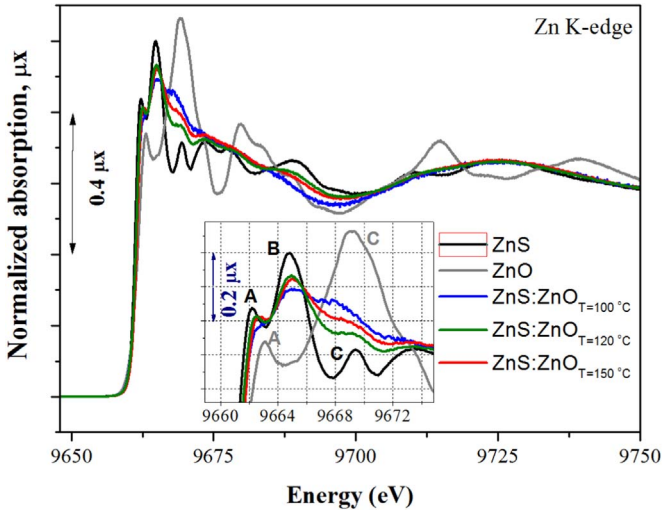

Fig. 5. Zn *K*-edge HERFD-XANES spectra collected for the samples synthesized at 100 °C (blue), 120 °C (green) and 150 °C (red), and for reference ZnO (grey) and ZnS (black) compounds. The inset reports a magnification of the post edge region where the main XANES features of the ZnS and ZnO references are labaled as A,B,C. (For interpretation of the references to color in this figure legend, the reader is referred to the web version of this article.).

3.6. EXAFS

Experimental amplitudes of phase corrected k^2-weighted FT of the Zn K-edge EXAFS collected in fluorescence mode for synthesized NPs in comparison with standard samples are shown in Fig. 7. For both samples synthesized at 120 °C and 150 °C one observes a lower coordination number in the 1st coordination shell compared to the reference ZnS samples due to a higher disorder of the structure and significant contribution of surface Zn atoms. Sharper and more

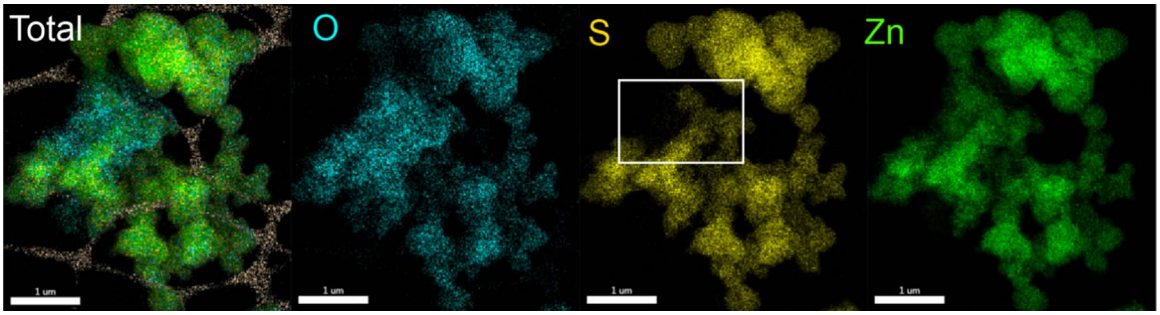

Fig. 4. STEM element selective mapping for the sample synthesized at 120 °C. White rectangle specify sulfur poor region.

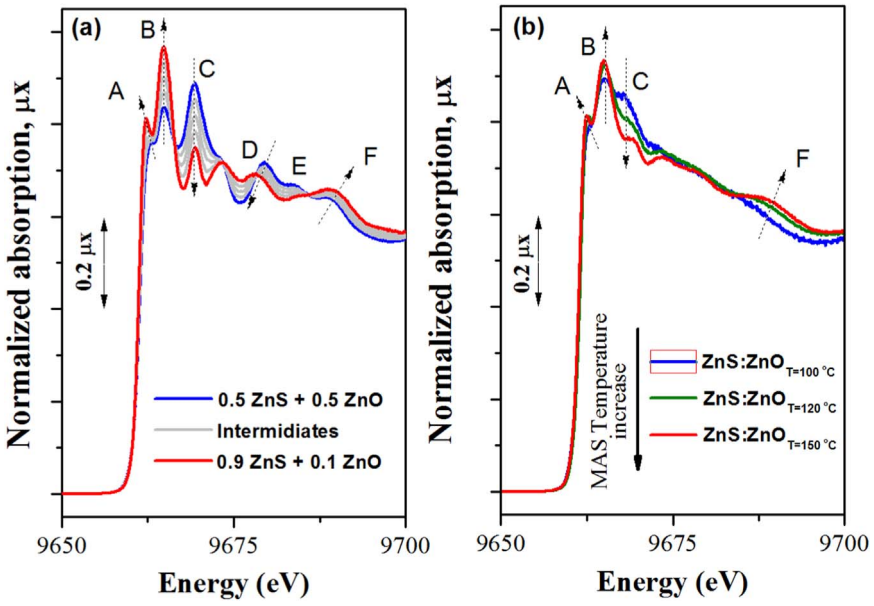

Fig. 6. (a) Zn K-edge HERFD-XANES spectra constructed as a superposition of ZnO and ZnS with different weight coefficients **(b)** Zn K-edge HERFD-XANES spectra collected on ZnS:ZnO samples synthesized at different temperatures (same spectra as in Fig. 5, reported in a larger energy range).

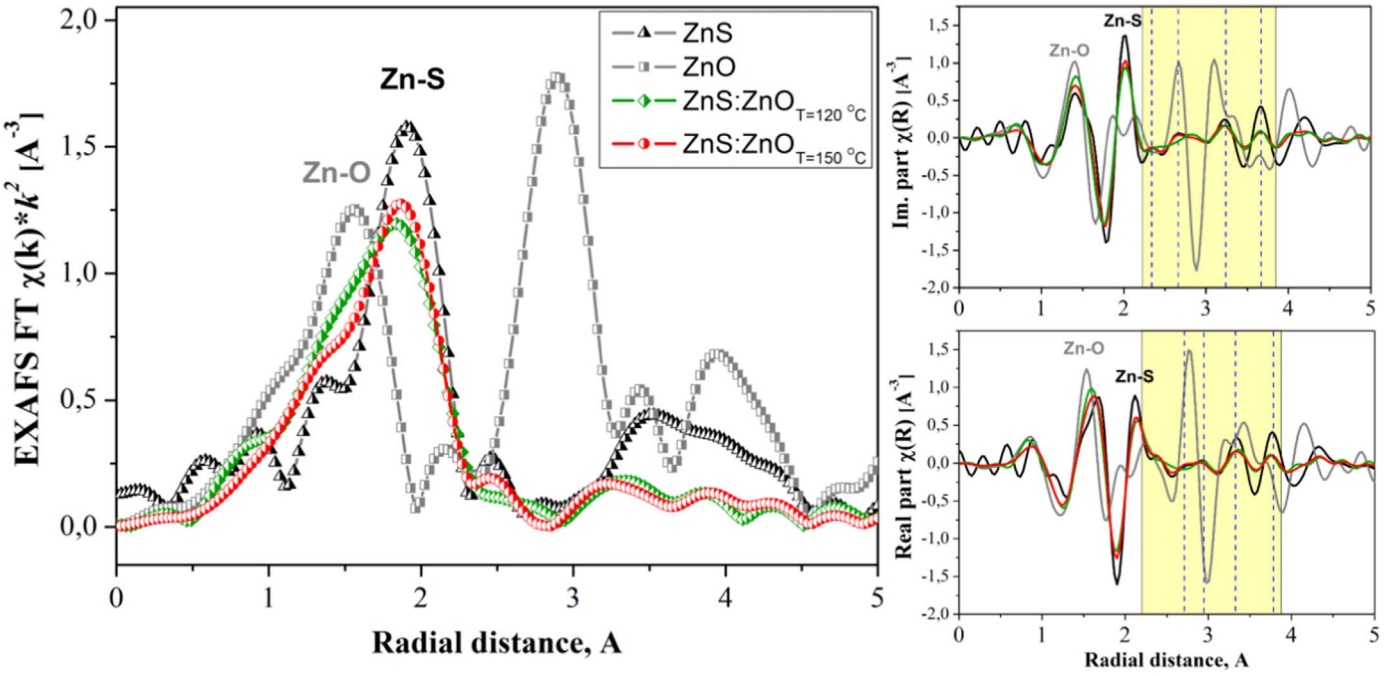

Fig. 7. Phase uncorrected Zn K-edge experimental **(a)** k^2-weighted FT-EXAFS amplitudes, **(b)** imaginary part FT-EXAFS signal, **(c)** real part of FT-EXAFS signal collected on synthesized samples in comparison with data obtained for hexagonal bulk zinc sulfide and zinc oxide.

localized peak corresponding to Zn-S scattering is observed for the sample synthesized at 150 °C (compare with the one synthesized at 120 °C) indicating that the dominant component is ZnS presence in a higher amount, which is in agreement with an XRPD analysis (See Section 3.2).

All FT-EXAFS are characterized by the main peak at R = 1.89 Å in phase uncorrected signal which corresponds to the Zn-S contribution. The shoulder at lower R-values evidences the existence of the Zn-O contribution, which is explicitly shown in imaginary part. The intensity of this contribution is lower than that of ZnS due to lower scattering amplitude of oxygen in comparison to sulfur, and to the lower fraction of ZnO phase as determined by XANES (See below Table 1). All the samples absolutely lack the 2nd shell contribution of the ZnO phase (in the 2.5 – 3.2 Å phase-uncorrected FT), while more distant shells of ZnS are still present; moreover, the imaginary and real parts of the FT EXAFS spectra in the whole 2.2 – 3.8 Å range has the same phase than that of ZnS.

The quantitate determination of the ZnO and ZnS phases from the EXAFS data is problematic due to the limited k-range, which leads to the fact that Zn-S and Zn-O contributions are not well resolved, causes instabilities of Fourier-analysis procedure, and limits the number of fitting parameters.

3.7. VtC-XES

VtC-XES normalized spectra obtained for the two samples synthesized at 120 °C and 150 °C in comparison with the data collected on ZnS and ZnO reference samples are presented in Fig. 8. The data

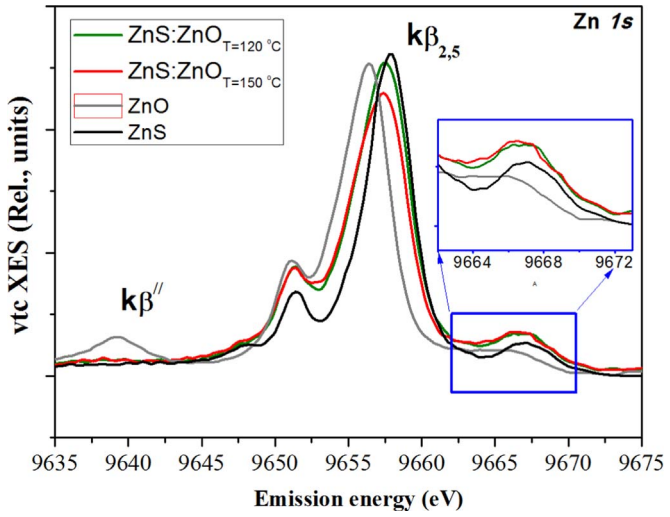

Fig. 8. VtC-XES K$\beta_{2,5}$ normalized spectra collected on samples synthesized at 120 °C and 150 °C in comparison with the data collected for reference ZnS and ZnO samples.

measured for ZnS and ZnO bulk system are in good agreement with experimental data very recently reported in the literature [87].

The whole complex profile of the K$\beta_{2,5}$ component and high energy satellite in particular (see blue rectangle in the Fig. 6) for the samples under study is very close to the similar features observed in the XES spectrum of ZnS. Looking carefully to the energy position of the maxima, it is evident that, in the XES spectra of the samples under study, they are slightly shifted towards the lower energy i.e. towards the position of corresponding peaks as observed for ZnO. The larger energy shift of K$\beta_{2,5}$ maximum of sample synthesized at 120 °C towards the lower energy is in good agreement with a higher concentration of ZnO in this sample derived by XANES LCF analysis. The superposition of VtC-XES data obtained for pure ZnS and ZnO phases taking into account weight coefficients obtained as a result of XANES LCF analysis provides a good fit of VtC-XES spectra for investigated samples, expecting low-energy satellite region (See Supp. Info Fig S5).

Low energy satellite referred to as K$\beta^{//}$, centered at 9639 eV is highly explicit in the spectra collected on ZnO bulk system and corresponds to the presence of a bulk Zn-O chemical bonding. This peak is absent in the spectrum of ZnS. It is apparently surprising to observe that for the spectra collected on ZnS:ZnO samples there are almost no features in this region. The reason of absence any spectral features for investigated samples in this energy region could be explained by considering that, even in pure ZnO, it is one order of magnitude less intense than the corresponding K$\beta_{2,5}$, implying that for samples having relatively low fraction of ZnO, its contribution could be overshadowed by the noise level. Besides VtC-XES features are very sensitive to the symmetry of bonding orbitals so they could be completely different for amorphous ZnO compared with a bulk material.

Summarizing, XES data could be considered as an additional experimental confirmation of qualitative estimation of ZnS/ZnO factional ratios for the materials under the study obtained by means of complementary HERFD-XANES and VtC-XES technique.

3.8. Summary

Taking into account that there is no evidence of crystalline ZnO presence obtained by XRPD study (see Section 3.2), however it is clearly seen by energy dispersive X-ray analysis (See Section 3.4) and X-ray absorption spectroscopy (See Section 3.5) that samples under the scope contains singnificant amount of oxidized phase we proposed that all samples represented by small ZnS NPs with a crystalline atomic ordering which could be capped by amorphous oxidized phase. This phase most likely is represented by zinc hydroxide which fills the interstitial space during agglomeration process. Upon drying of the synthesis product zinc hydroxide is converted into amorphous ZnO phase (See Section 3.1) with a local atomic structure similar to crystalline ZnO. The samples under the scope of this study have a core-shell like structural morphology, but it could not be referred to as core-shell NPs due to agglomeration process.

The solubility constants of ZnS ($2.2\cdot10^{-17}$ [88]) is 6 orders less than one for ZnO ($2.2\cdot10^{-23}$ [89]). Due to the fact that the solubility constant for ZnS is low, ZnS precipitation can take place even at the lowest Zn^{2+} and S^{2-} ion concentration. It provides the condition for predominantly formation of the sulfide phase and transition from oxide to sulfide phases if there is enough concentration of the sulfide anion S^{2-}. At the beginning of the reaction there are no S^{2-} anions for the formation of ZnS but at these conditions the formation of $Zn(OH)_2$ is favorable.

As soon as the hydrolysis of the thiourea is occurs, sulfide anions appear in the solution, which causes precipitation ZnS by the reaction between soluble form of the zinc and precipitated $Zn(OH)_2$. The proposed reaction mechanism could be proved by the changes of ZnS:ZnO related with changes of T_{MAS}. The increase of the synthesis temperature promotes more effective hydrolysis of the thiourea as indicated by the higher content of the ZnS fraction in the NPs synthesized at a higher temperature.

4. Conclusions

XRPD full profile analysis shows the formation of small hexagonal ZnS crystallites however electron diffraction data also indicates the presence of cubic ZnS. XRPD peaks broadening analysis demonstrate that synthesized samples are represented by small ZnS crystallites and the averaged size belongs to the range of 2.7–3.7 Å that increases with increasing T_{MAS} (Microwave Assisted Synthesis Temperature). However, HR-TEM shows formation of relatively big conglomerates with a size distribution in the 60–200 nm range. Theoretical estimation of agglomeration number reveals that NPs synthesized at a higher temperature more prone to agglomeration process. The higher value of agglomeration number n = 513 was obtained for the sample synthesized at 150 °C. EDX analysis demonstrates homogeneous distribution of O and S atoms across the conglomerates and among them. Analysis of HERFD-XANES data unambiguously reveals a presence of significant amount of ZnO phase, which strongly correlates with a T_{MAS}. The qualitative discussion of the real and imaginary parts of the k^2-weighted FT-EXAFS signals is in a good agreement with both diffraction and HERFD-XANES analyses, showing a small perturbation of the Zn-S dominant first shell peak in its low R-region due to the presence of a minor fraction of Zn-O bonds. In the higher shell region the only contribution from the ZnS phase is present, supporting the hypothesis of a very thin amorphous ZnO layer. The results of XANES linear combination analysis depict the decreasing of ZnO fraction with an increasing of T_{MAS}. The ratios ZnS:ZnO derived by XANES LCF analysis are in a good agreement with S:O ratio obtained by EDX. The higher ZnS fraction ~ 77% was obtained for the NPs synthesized at 150 °C. VtC-XES data could be considered as a complementary technique which also demonstrates the ZnO presence in the samples and confirm the results of XANES LCF fit.

This temperature-dependent behavior could be explained by the kinetic mechanism of the synthesis reactions. In particular, increase of the synthesis temperature promotes a more effective hydrolysis of the thiourea which is the major fabricator (carrier) of sulfide anions in the reaction solution. Free sulfide anions interacting with a soluble form of the zinc and/or amorphous phase of the precipitate $Zn(OH)_2$ forms ZnS NPs, which undergo agglomeration and form relatively big conglomerates. Zinc hydroxide remains in all the samples after synthesis and forms an amorphous ZnO phase most likely distributed on the surface of small ZnS crystallites and in the interstitial space upon agglomeration small NPs into bigger ones.

Acknowledgement

Authors thank the Ministry of Education and Science of the Russian Federation for the award of grant 16.3871.2017/4.6 ("Picometre diagnostics of parameters of 3D atomic structure of nanomaterials on the basis of XANES spectroscopy").

The experiment was performed on beamline ID26 at the European Synchrotron Radiation Facility (ESRF), Grenoble, France. We are grateful to Sara Lafuerza at the ESRF for providing assistance in using ID26 beamline.

Appendix A. Supporting information

Supplementary data associated with this article can be found in the online version at doi:10.1016/j.jssc.2018.03.008.

References

[1] K. Chatterjee, S. Sarkar, K.J. Rao, S. Paria, Core/shell nanoparticles in biomedical applications, Adv. Colloid Interface Sci. 209 (2014) 8–39.
[2] D. Vasudevan, R.R. Gaddam, A. Trinchi, I. Cole, Core-shell quantum dots: properties and applications, J. Alloy. Compd. 636 (2015) 395–404.
[3] S. Nagarajan, Z. Yong, Use of core/shell structured nanoparticles for biomedical applications, Recent Pat. Biomed. Eng. 1 (2008) 34–42.
[4] V. Biju, T. Itoh, A. Anas, A. Sujith, M. Ishikawa, Semiconductor quantum dots and metal nanoparticles: syntheses, optical properties, and biological applications, Anal. Bioanal. Chem. 391 (2008) 2469–2495.
[5] M.F. Frasco, N. Chaniotakis, Semiconductor quantum dots in chemical sensors and biosensors, Sensors 9 (2009) 7266–7286.
[6] A.A. Guda, M.A. Soldatov, A.V. Soldatov, Group III–V and II–VI quantum dots and nanoparticles, in: C.S. Schnohr, M.C. Ridgway (Eds.), X-Ray Absorption Spectroscopy of Semiconductors, Springer Berlin Heidelberg, Berlin, Heidelberg, 2015, pp. 247–268.
[7] R. Gill, M. Zayats, I. Willner, Semiconductor quantum dots for bioanalysis, Angew. Chem. -Int. Ed. 47 (2008) 7602–7625.
[8] Z.W. Jin, N. Hildebrandt, Semiconductor quantum dots for in vitro diagnostics and cellular imaging, Trends Biotechnol. 30 (2012) 394–403.
[9] T. Pons, N. Lequeux, B. Mahler, S. Sasnouski, A. Fragola, B. Dubertret, Synthesis of Near-infrared-emitting, water-soluble CdTeSe/CdZnS core/shell quantum dots, Chem. Mat. 21 (2009) 1418–1424.
[10] J. Zhou, Y. Yang, C.Y. Zhang, Toward biocompatible semiconductor Quantum Dots: from biosynthesis and bioconjugation to biomedical application, Chem. Rev. 115 (2015) 11669–11717.
[11] A.J. Nozik, Spectroscopy and hot electron relaxation dynamics in semiconductor quantum wells and quantum dots, Annu. Rev. Phys. Chem. 52 (2001) 193–231.
[12] P. Kambhampati, Unraveling the the structure and dynamics of excitons in semiconductor quantum dots, Acc. Chem. Res. 44 (2011) 1–13.
[13] D.J. Mowbray, M.S. Skolnick, New physics and devices based on self-assembled semiconductor quantum dots, J. Phys. D.-Appl. Phys. 38 (2005) 2059–2076.
[14] A.D. Yoffe, Semiconductor quantum dots and related systems: electronic, optical, luminescence and related properties of low dimensional systems, Adv. Phys. 50 (2001) 1–208.
[15] C. Lamberti, The use of synchrotron radiation techniques in the characterization of strained semiconductor heterostructures and thin films, Surf. Sci. Rep. 53 (2004) 1–197.
[16] C. Lamberti, G. Agostini, Characterization of Semiconductor Heterostructures and Nanostructures, 2nd ed., Elsevier Science Bv, Amsterdam, 2013.
[17] R. Freeman, I. Willner, Optical molecular sensing with semiconductor quantum dots (QDs), Chem. Soc. Rev. 41 (2012) 4067–4085.
[18] N. Fuke, L.B. Hoch, A.Y. Koposov, V.W. Manner, D.J. Werder, A. Fukui, N. Koide, H. Katayama, M. Sykora, CdSe quantum-dot-sensitized solar cell with similar to 100% internal quantum efficiency, ACS Nano 4 (2010) 6377–6386.
[19] K.S. Leschkies, A.G. Jacobs, D.J. Norris, E.S. Aydil, Nanowire-quantum-dot solar cells and the influence of nanowire length on the charge collection efficiency, Appl. Phys. Lett. 95 (2009) 193103.
[20] A.J. Nozik, M.C. Beard, J.M. Luther, M. Law, R.J. Ellingson, J.C. Johnson, Semiconductor quantum dots and quantum dot arrays and applications of multiple exciton generation to third-generation photovoltaic solar cells, Chem. Rev. 110 (2010) 6873–6890.
[21] M. Navaneethan, J. Archana, K.D. Nisha, Y. Hayakawa, S. Ponnusamy, C. Muthamizhchelvan, Synthesis of highly size confined ZnS quantum dots and its functional characteristics, Mater. Lett. 68 (2012) 78–81.
[22] K.F. Lin, H.M. Cheng, H.C. Hsu, L.J. Lin, W.F. Hsieh, Band gap variation of size-controlled ZnO quantum dots synthesized by sol-gel method, Chem. Phys. Lett. 409 (2005) 208–211.
[23] B. Bhattacharjee, D. Ganguli, S. Chaudhuri, A.K. Pal, Synthesis and optical characterization of sol-gel derived zinc sulphide nanoparticles confined in amorphous silica thin films, Mater. Chem. Phys. 78 (2003) 372–379.
[24] C. Feldmann, C. Metzmacher, Polyol mediated synthesis of nanoscale MS particles (M = Zn, Cd, Hg), J. Mater. Chem. 11 (2001) 2603–2606.
[25] H.J. Byun, J.C. Lee, H. Yang, Solvothermal synthesis of InP quantum dots and their enhanced luminescent efficiency by post-synthetic treatments, J. Colloid Interface Sci. 355 (2011) 35–41.
[26] R. Shahid, M.S. Toprak, M. Muhammed, Microwave-assisted low temperature synthesis of wurtzite ZnS quantum dots, J. Solid State Chem. 187 (2012) 130–133.
[27] D.E. Clark, D.C. Folz, J.K. West, Processing materials with microwave energy, Mater. Sci. Eng. A-Struct. Mater. Prop. Microstruct. Process. 287 (2000) 153–158.
[28] E.T. Thostenson, T.W. Chou, Microwave processing: fundamentals and applications, Compos. Pt. A-Appl. Sci. Manuf. 30 (1999) 1055–1071.
[29] S. Cho, S.H. Jung, K.H. Lee, Morphology-controlled growth of ZnO nanostructures using microwave irradiation: from basic to complex structures, J. Phys. Chem. C 112 (2008) 12769–12776.
[30] Z.P. Zeng, C.S. Garoufalis, A.F. Terzis, S. Baskoutas, Linear and nonlinear optical properties of ZnO/ZnS and ZnS/ZnO core shell quantum dots: effects of shell thickness, impurity, and dielectric environment, J. Appl. Phys. 114 (2013) 023510.
[31] X.S. Fang, Y. Bando, U.K. Gautam, T.Y. Zhai, H.B. Zeng, X.J. Xu, M.Y. Liao, D. Golberg, ZnO and ZnS nanostructures: ultraviolet-light emitters, lasers, and sensors, Crit. Rev. Solid State Mat. Sci. 34 (2009) 190–223.
[32] S.H. Ko, D. Lee, H.W. Kang, K.H. Nam, J.Y. Yeo, S.J. Hong, C.P. Grigoropoulos, H.J. Sung, Nanoforest of hydrothermally grown hierarchical ZnO nanowires for a high efficiency dye-sensitized solar cell, Nano Lett. 11 (2011) 666–671.
[33] J. Lahiri, M. Batzill, Surface functionalization of ZnO photocatalysts with monolayer ZnS, J. Phys. Chem. C 112 (2008) 4304–4307.
[34] M. Cristea, E.C. Niculescu, Hydrogenic impurity states in CdSe/ZnS and ZnS/CdSe core-shell nanodots with dielectric mismatch, Eur. Phys. J. B 85 (2012) 191.
[35] M. Rajalakshmi, S. Sohila, R. Ramesh, G.M. Bhalerao, Enhancement of photoluminescence in ZnS/ZnO quantum dots interfacial heterostructures, Mater. Res. Bull. 47 (2012) 2668–2672.
[36] L.P. Balet, S.A. Ivanov, A. Piryatinski, M. Achermann, V.I. Klimov, Inverted core/shell nanocrystals continuously tunable between type-I and type-II localization regimes, Nano Lett. 4 (2004) 1485–1488.
[37] J.H. Yang, J.A. Cao, L.L. Yang, Y.J. Zhang, Y.X. Wang, X.Y. Liu, D.D. Wang, M.B. Wei, M. Gao, J.H. Lang, Fabrication and photoluminescence of ZnS:$Mn^{(2+)}$ nanowires/ZnO quantum dots/$SiO_{(2)}$ heterostructure, J. Appl. Phys. 108 (2010) 044304.
[38] J. Schrier, D.O. Demchenko, L.W. Wang, Optical properties of ZnO/ZnS and ZnO/ZnTe heterostructures for photovoltaic applications, Nano Lett. 7 (2007) 2377–2382.
[39] W.N. Jia, B.X. Jia, H.M. Lin, F.Y. Qu, X. Wu, J.J. Jiang, Solution growth and optical property of ZnS/ZnO microspheres, Micro Nano Lett. 6 (2011) 633–635.
[40] F.J. Wang, J. Liu, Z.J. Wang, A.J. Lin, H. Luo, X.B. Yu, Interfacial heterostructure phenomena of highly luminescent ZnS/ZnO quantum dots, J. Electrochem. Soc. 158 (2011) 30–34.
[41] (a) A.L. Bugaev, A.A. Guda, K.A. Lomachenko, V.V. Shapovalov, A. Lazzarini, J.G. Vitillo, L.A. Bugaev, E. Groppo, R. Pellegrini, A.V. Soldatov, J.A. van Bokhoven, C. Lamberti, Core-Shell structure of palladium hydride nanoparticles revealed by combined X-ray absorption spectroscopy and X-ray diffraction, J. Phys. Chem. C 121 (2017) 18202–18213;

(b) A.L. Bugaev, O.A. Usoltsev, A.A. Guda, K.A. Lomachenko, I.A. Punkin, Yu.V. Rusalev, H. Emerich, E. Groppo, R. Pellegrini, A.V. Soldatov, J.A. van Bokhoven, C. Lamberti, Palladium carbide and hydride formation in the bulk and at the surface of palladium nanoparticles, J. Phys. Chem. C (2018). http://dx.doi.org/10.1021/acs.jpcc.7b11473 (in press);

(c) A.L. Bugaev, O.A. Usoltsev, A. Lazzarini, K.A. Lomachenko, A.A. Guda, R. Pellegrini, M. Carosso, J. Vitillo, E. Groppo, J. van Bokhoven, A.V. Soldatov, C. Lamberti, Time-resolved operando studies of carbon supported Pd nanoparticles under hydrogenation reactions by X-ray diffraction and absorption, Faraday Discuss. (2018). http://dx.doi.org/10.1039/C7FD00211D (in press).
[42] J.J. Rehr, R.C. Albers, Theoretical approaches to x-ray absorption fine structure, Rev. Mod. Phys. 72 (2000) 621–654.
[43] L. Mino, G. Agostini, E. Borfecchia, D. Gianolio, A. Piovano, E. Gallo, C. Lamberti, Low-dimensional systems investigated by x-ray absorption spectroscopy: a selection of 2D, 1D and 0D cases, J. Phys. D.-Appl. Phys. 46 (2013) 423001.
[44] A.A. Guda, N. Smolentsev, M. Rovezzi, E.M. Kaidashev, V.E. Kaydashev, A.N. Kravtsova, V.L. Mazalova, A.P. Chaynikov, E. Weschke, P. Glatzel, A.V. Soldatov, Spin-polarized electronic structure of the core-shell ZnO/ZnO:Mn nanowires probed by X-ray absorption and emission spectroscopy, J. Anal. At. Spectrom. 28 (2013) 1629–1637.
[45] A. Rogalev, K. Ollefs, F. Wilhelm, X-ray magnetic circular dichroism, in: J.A. van Bokhoven, C. Lamberti (Eds.), X-Ray Absorption and X-Ray Emission Spectroscopy: Theory and Applications, John Wiley & Sons, Chichester (UK), 2016, pp. 671–694.
[46] A.V. Kolobov, H. Oyanagi, K. Tanaka, K. Tanaka, Structural study of amorphous selenium by in situ EXAFS: observation of photoinduced bond alternation, Phys. Rev. B 55 (1997) 726–734.
[47] L.A. Bugaev, A.P. Sokolenko, H.V. Dmitrienko, A.M. Flank, Fourier filtration of XANES as a source of quantitative information of interatomic distances and coordination numbers in crystalline minerals and amorphous compounds, Phys. Rev. B 65 (2002) 8.
[48] A. Tougerti, E. Berrier, A.S. Mamede, C. La Fontaine, V. Briois, Y. Joly, E. Payen, J.F. Paul, S. Cristol, Synergy between XANES spectroscopy and DFT to elucidate the amorphous structure of heterogeneous catalysts: TiO_2-supported molybdenum oxide catalysts, Angew. Chem. -Int. Ed. 52 (2013) 6440–6444.
[49] A. Filipponi, EXAFS for liquids, J. Phys. -Condens. Matter 13 (2001) R23–R60.

[50] A. Filipponi, P. D'Angelo, XAS in liquid systems, in: J.A. van Bokhoven, C. Lamberti (Eds.), X-Ray Absorption and X-Ray Emission Spectroscopy: Theory and Applications, John Wiley & Sons, Chichester (UK), 2016, pp. 745–771.
[51] A. Martini, E. Borfecchia, K.A. Lomachenko, I.A. Pankin, C. Negri, G. Berlier, P. Beato, H. Falsig, S. Bordiga, C. Lamberti, Composition-driven Cu-speciation and reducibility in Cu-CHA zeolite catalysts: a multivariate XAS/FTIR approach to complexity, Chem. Sci. 8 (2017) 6836–6851.
[52] C. Paolucci, A.A. Parekh, I. Khurana, J.R. Di Iorio, H. Li, J.D.A. Caballero, A.J. Shih, T. Anggara, W.N. Delgass, J.T. Miller, F.H. Ribeiro, R. Gounder, W.F. Schneider, Catalysis in a cage: condition-dependent speciation and dynamics of exchanged Cu cations in SSZ-13 zeolites, J. Am. Chem. Soc. 138 (2016) 6028–6048.
[53] K.A. Lomachenko, E. Borfecchia, C. Negri, G. Berlier, C. Lamberti, P. Beato, H. Falsig, S. Bordiga, The Cu-CHA $deNO_{(x)}$ catalyst in action: temperature-dependent NH_3-Assisted selective catalytic reduction monitored by operando XAS and XES, J. Am. Chem. Soc. 138 (2016) 12025–12028.
[54] C.H.M. van Oversteeg, H.Q. Doan, F.M.F. de Groot, T. Cuk, In situ X-ray absorption spectroscopy of transition metal based water oxidation catalysts, Chem. Soc. Rev. 46 (2017) 102–125.
[55] S.R. Bare, T. Ressler, Characterization of catalysts in reactive atmospheres by x-ray absorption spectroscopy, Adv. Catal. 52 (2009) 339–465.
[56] C. Lamberti, A. Zecchina, E. Groppo, S. Bordiga, Probing the surfaces of heterogeneous catalysts by in situ IR spectroscopy, Chem. Soc. Rev. 39 (2010) 4951–5001.
[57] G.N. George, B. Hedman, K.O. Hodgson, An edge with XAS, Nat. Struct. Biol. 5 (1998) 645–647.
[58] A.N. Kravtsova, A.P. Budnik, I.A. Pankin, T.A. Lastovina, A.L. Bugaev, L.D. Popov, M.A. Soldatov, V.V. Butova, A.V. Soldatov, Local atomic and electronic structure of quantum dots based on Mn- and Co-doped ZnS, J. Struct. Chem. 58 (2017) 45–52.
[59] A.N. Kravtsova, I.A. Pankin, A.P. Budnyk, V.V. Butova, T.A. Lastovina, A.V. Soldatov, Synthesis and structure modeling of ZnS based quantum dots, J. Struct. Chem. 57 (2016) 926–933.
[60] U. Bergmann, P. Glatzel, X-ray emission spectroscopy, Photosynth. Res. 102 (2009) 255–266.
[61] A. Kotani, S. Shin, Resonant inelastic x-ray scattering spectra for electrons in solids, Rev. Mod. Phys. 73 (2001) 203–246.
[62] A. Nilsson, L.G.M. Pettersson, Chemical bonding on surfaces probed by X-ray emission spectroscopy and density functional theory, Surf. Sci. Rep. 55 (2004) 49–167.
[63] P. Glatzel, U. Bergmann, High resolution 1s core hole X-ray spectroscopy in 3d transition metal complexes - electronic and structural information, Coord. Chem. Rev. 249 (2005) 65–95.
[64] J. Singh, C. Lamberti, J.A. van Bokhoven, Advanced X-ray absorption and emission spectroscopy: in situ catalytic studies, Chem. Soc. Rev. 39 (2010) 4754–4766.
[65] E. Gallo, P. Glatzel, Valence to core X-ray emission spectroscopy, Adv. Mater. 26 (2014) 7730–7746.
[66] C.J. Pollock, S. DeBeer, Insights into the geometric and electronic structure of transition metal centers from valence-to-core X-ray emission, Spectrosc. Acc. Chem. Res. 48 (2015) 2967–2975.
[67] P. Glatzel, R. Alonso-Mori, D. Sokaras, Hard X-ray photon-in/photon-out spectroscopy: instrumentation, theory and applications, in: J.A. van Bokhoven, C. Lamberti (Eds.), X-Ray Absorption and X-Ray Emission Spectroscopy: Theory and Applications, John Wiley & Sons, Chichester (UK), 2016, pp. 125–153.
[68] T. Gunter, D.E. Doronkin, H.W.P. Carvalho, M. Casapu, J.D. Grunwaldt, Iop, HERFD-XANES and XES as complementary operando tools for monitoring the structure of Cu-based zeolite catalysts during NOx-removal by ammonia SCR, in: Proceedings of the 16th International Conference on X-Ray Absorption Fine Structure, Iop Publishing Ltd, Bristol, 2016, pp. 012071.
[69] C.W. Andersen, E. Borfecchia, M. Bremholm, M.R.V. Jorgensen, P.N.R. Vennestrom, C. Lamberti, L.F. Lundegaard, B.B. Iversen, Redox-driven migration of copper ions in the Cu-CHA zeolite as shown by the in situ PXRD/XANES technique, Angew. Chem. -Int. Ed. 56 (2017) 10367–10372.
[70] A. Krezel, W. Maret, The biological inorganic chemistry of zinc ions, Arch. Biochem. Biophys. 611 (2016) 3–19.
[71] V. Petricek, M. Dusek, L. Palatinus, Crystallographic computing system JANA2006: general features, Z. Krist. -Cryst. Mater. 229 (2014) 345–352.
[72] A. Lida, T. Noma, Correction of the self-absorption effect in fluorescence X-ray absorption fine-structure, Jpn. J. Appl. Phys. Part 1 - Regul. Pap. Short. Notes Rev. Pap. 32 (1993) 2899–2902.
[73] C.H. Booth, F. Bridges, Improved self-absorption correction for fluorescence measurements of extended X-ray absorption fine-structure, Phys. Scr. T115 (2005) 202–204.
[74] E. Gallo, C. Lamberti, P. Glatzel, Investigation of the valence electronic states of Ti(IV) in Ti silicalite-1 coupling X-ray emission spectroscopy and density functional calculations, Phys. Chem. Chem. Phys. 13 (2011) 19409–19419.
[75] J.H. Jang, J.H. Park, O.S. G, Effects of dodecyl sulfate anionic surfactants on the crystal growth of ZnO through hydrothermal process, J. Ceram. Process. Res. 10 (2009) 783–790.
[76] J.A. Garcia-Valenzuela, Simple thiourea hydrolysis or intermediate complex mechenism taking up the formation of metal sulfides from metal-thiourea alkaline solutions, comments, Inorg. Chem. 37 (2017) 99–115.
[77] T.V. Vinogradova, V.F. Markov, L.N. Maskaeva, Temperature dependence of constants of thiourea hydrolytic decomposition and cyanamide. stepwise ionization, Russ. J. Gen. Chem. 80 (2010) 2341–2346.
[78] G. Hodes, Chemical solution deposition of semiconductor films., in, CRC Press, Boca Raton, 2002.
[79] V.F.M. Markov, L.N. Ivanov, P.N. Gidrokhimicheskoe, osazhdenie plenok sul'fidov metallov: modelirovanie i eksperiment, in: Y.N. Makurin (Ed.)UrO RAN, Yekaterinburg, Russia, 2006.
[80] E.H. Kisi, M.M. Elcombe, Upsilon-parameters for the wurtzite structure of ZnS and ZnO using powder neutron-diffraction, Acta Crystallogr. Sect. C.-Cryst. Struct. Commun. 45 (1989) 1867–1870.
[81] E. Wetterskog, C.W. Tai, J. Grins, L. Bergstrom, G. Salazar-Alvarez, Anomalous magnetic properties of nanoparticles arising from defect structures: topotaxial oxidation of $Fe_{1-x}O$ vertical bar Fe_3-delta O_4 core vertical bar shell nanocubes to single-phase particles, ACS Nano 7 (2013) 7132–7144.
[82] A.L. Patterson, The Scherrer Formula for X-ray particle size determination, Phys. Rev. 56 (1939) 978–982.
[83] R. Pellegrini, G. Agostini, E. Groppo, A. Piovano, G. Leofanti, C. Lamberti, 0.5 wt% Pd/C catalyst for purification of terephthalic acid: irreversible deactivation in industrial plants, J. Catal. 280 (2011) 150–160.
[84] H.R. Shakur, A detailed study of physical properties of ZnS quantum dots synthesized by reverse micelle method, Phys. E 44 (2011) 641–646.
[85] J.M. Nedeljkovic, R.C. Patel, P. Kaufman, C. Joycepruden, N. Oleary, Synthesis and optical-properties of quantum-size metal sulfide particles in aqueous-solution, J. Chem. Educ. 70 (1993) 342–344.
[86] B. Ravel, M. Newville, Athena, Artemis, Hephaestus: data analysis for X-ray absorption spectroscopy using IFEFFIT, J. Synchrotron Radiat. 12 (2005) 537–541.
[87] D.R. Mortensen, G.T. Seidler, J.J. Kas, N. Govind, C.P. Schwartz, S. Pemmaraju, D.G. Prendergast, Benchmark results and theoretical treatments for valence-to-core x-ray emission spectroscopy in transition metal compounds, Phys. Rev. B 96 (2017) 125136.
[88] T.P. Dirkse, The solubility product constant of ZnO, J. Electrochem. Soc. 133 (1986) 1656–1657.
[89] A.W. Adamson, Advanced inorganic chemistry, in: f.A. Cotton, G. Wilkinson (Eds.), Inorg. Chem. 2 (1963), 1963 (665-665).